communications chemistry

Article

https://doi.org/10.1038/s42004-024-01284-2

On-surface synthesis of porous graphene nanoribbons mediated by phenyl migration

César Moreno [1,2] ✉, Xabier Diaz de Cerio [3], Maria Tenorio [2,8], Fei Gao[3], Manuel Vilas-Varela[4], Ane Sarasola[3,5], Diego Peña [4] ✉, Aran Garcia-Lekue [3,6] ✉ & Aitor Mugarza [2,7] ✉

Advancements in the on-surface synthesis of atomically precise graphene nanostructures are propelled by the introduction of innovative precursor designs and reaction types. Until now, the latter has been confined to cross-coupling and cyclization reactions that involve the cleavage of specific atoms or groups. In this article, we elucidate how the migration of phenyl substituents attached to graphene nanoribbons can be harnessed to generate arrays of [18]-annulene pores at the edges of the nanostructures. This sequential pathway is revealed through a comprehensive study employing bond-resolved scanning tunneling microscopy and ab-initio computational techniques. The yield of pore formation is maximized by anchoring the graphene nanoribbons at steps of vicinal surfaces, underscoring the potential of these substrates to guide reaction paths. Our study introduces a new reaction to the on-surface synthesis toolbox along with a sequential route, altogether enabling the extension of this strategy towards the formation of other porous nanostructures.

Since the pioneering synthesis of 7-atom wide armchair graphene nanoribbons (GNRs) on a Au(111) surface[1], the field of on-surface synthesis (OSS) has witnessed remarkable progress, successfully generating a myriad of GNRs with diverse structures[2,3]. The ongoing advancements in this domain are marked by a transition towards higher complexities, such as heterostructures, superlattices, and nanopores. The latter, crucial for applications ranging from quantum electronics[4] to gas separation[5], water purification[6], chemical sensing[7], or ion transport[8], can be incorporated through various methods. For instance, lateral coupling of prealigned GNRs comprising sidegroups acting as coupling bridges can result in two-dimensional nanoporous structure[9–11]. We recently showcased the versatility of this molecular bridge engineering approach by synthesizing lateral heterostructure superlattices[12] and nanoporous graphene (NPG) with customizable phenylated bridges[13]. Lower dimensional nanoporous structures like quantum dots[14–20] or GNRs[21–26] have also been synthesized using different reactions. In the case of GNRs, all reported structures rely on the Ullmann coupling of rigid building blocks, with one exception where Ullmann polymerization is facilitated by phenylene rotation followed by dehydrogenation cross-linking for the completion of the nanoporous ribbon[21]. Recent studies have reported the observation of phenyl migration in surface-assisted, thermally induced internal transformations of molecules[27,28]. The most recent study by Ruan et al. showed that a highly selective intermediate phenyl migration reaction can still yield a multitude of final products[28], emphasizing the necessity for selectivity throughout the entire reaction path to implement phenyl migration in on-surface nanostructure synthesis. In this study, we meticulously orchestrated Ullmann coupling, cyclodehydrogenation, phenyl migration, and aryl-aryl intraribbon dehydrogenative coupling reactions in a sequential manner to achieve the desired atomically precise porous GNRs. The distinct thermal windows of the reaction steps enable the generation of well-defined intermediates, rendering our growth protocol a viable approach for synthesizing other complex graphene nanoarchitectures.

Results

The building block of the on-surface synthesized porous GNRs presented here is 2,2'-di([1,1'-biphenyl]-4-yl)-10,10'-dibromo-9,9'-bianthracene

[1]Departamento de Ciencias de la Tierra y Fisica de la Materia Condensada, Universidad de Cantabria, Santander, Spain. [2]Catalan Institute of Nanoscience and Nanotechnology (ICN2), CSIC and BIST, Bellaterra, 08193 Barcelona, Spain. [3]Donostia International Physics Center, San Sebastian, Spain. [4]Centro de Investigación en Química Biolóxica e Materiais Moleculares (CIQUS) and Departamento de Química Orgánica, Universidade de Santiago de Compostela, Santiago de Compostela, Spain. [5]Departamento de Física Aplicada, Universidad del País Vasco/Euskal Herriko Unibertsitatea (UPV/EHU), Donostia, Spain. [6]Ikerbasque, Basque Foundation for Science, Bilbao, Spain. [7]ICREA—Institució Catalana de Recerca i Estudis Avançats, 08010 Barcelona, Spain. [8]Present address: Instituto Madrileño de Estudios Avanzados en Nanociencia (IMDEA Nanoscience), 28049 Madrid, Spain. ✉e-mail: cesar.moreno@unican.es; diego.pena@usc.es; wmbgalea@ehu.eus; aitor.mugarza@icn2.cat

(DBP-DBBA), a biantracene derivative that was prepared by solution chemistry following a previously reported procedure[13]. The OSS carried out in ultra-high vacuum conditions, summarized in Fig. 1, initiates with the deposition of the DBP-DBBA precursor (Fig. 1a) on the Au(111) surface held at room temperature. Subsequent annealing to $T_1 = 200$ °C induces thermal C-Br homolytic cleavage, generating radicals that cross-couple to form one-dimensional polymeric chains through the well-established Ullmann coupling reaction. A second annealing step at $T_2 = 400$ °C transforms the polymers into GNRs by undergoing internal cyclodehydrogenations, resulting in a planarized structure with a hexagonal lattice of aromatic rings characteristic of graphene (Fig. 1b). The inner phenylene rings of the peripheral bisphenyl groups fuse into the aromatic backbone, introducing a periodic modulation of the ribbon width with alternating pairs of 7 and 13 carbon atoms, a structure denoted as 7-13-AGNR in prior studies[9,29]. The outermost phenyl rings, however, remain single bonded, defining the overall ribbon structure as a phenylated Ph-7-13-AGNR. When individual Ph-7-13-AGNRs are aligned and free to laterally diffuse, annealing to higher temperatures induces a dehydrogenative cross-coupling reaction, fusing GNRs to form NPG with bisphenylene bridges[13]. However, if the lateral coupling is inhibited, a new reaction path opens with a threshold temperature of $T_3 = 450$ °C (Fig. 1c). In this scenario, a phenyl migrates to the neighboring equivalent position of the fused benzene in a first step, and the proximity with the adjacent phenyl triggers a dehydrogenative cross-coupling that leads to the formation of [18]-annulene pores.

Figure 2 depicts representative topographic STM images capturing the onset of the phenyl migration after post-annealing a sample containing Ph-7-13-AGNRs to $T = 450$ °C. In the majority of regions on the flat terraces, prealigned ribbons appear laterally fused, forming NPG stripes as the ones displayed in Fig. 2a. However, at the edges of the stripes, the side phenyl groups cannot couple and undergo distinct transformations. In small, disordered regions found at domain boundaries of GNR arrays, the anchoring of ribbons promotes similar transformations in isolated GNRs, as illustrated in Fig. 2b. Bond-resolved STM (BR-STM) images as the ones shown in Fig. 2c, d reveal that all observed transformations are assisted by a phenyl migration. In most cases, the migration occurs locally only for one phenyl and between the two equivalent peripheral positions of the fused benzene (C_2 and C_3 in Fig. 2e). This migration leads to the formation of [18]-annulene pores through the dehydrogenative *meta* coupling of adjacent phenyls (**1** in Fig. 2c). Eventually, the migrated phenyl does not find a confronting counterpart to close the pore (**1'** in Fig. 2c), either because the latter is already incorporated in an annulene pore, or due to the presence of a defective adjacent site or a ribbon termination. It is noteworthy that, while local configurations with coincident **1** and **1'** at opposing sides could also be attributed to the Ullmann coupling of monomers of opposite chirality, this possibility is ruled out by steric hindrance arguments at the polymeric phase (see Fig. S1), which imposes a staggering sequence of anthracenes that can only be achieved by a homochiral polymerization. This is confirmed by the absence of heterochiral units in the poly-DBBA chains imaged by STM in our previous studies[13]. A second type of migration can also occur from C_2/C_3 towards the triple bay area sites C_1/C_4, resulting in the fusion of the phenyl in the backbone through a triple dehydrogenative coupling (**2** in Fig. 2d). However, this pathway is significantly inhibited by the steric hindrance and energy cost associated with the cleavage of six C-H bonds. Overall, our statistical analysis of over 250 migrated phenyls reveals a selectivity towards the [18]-annulene pore formation path, measured as $\mathbf{1}/(\mathbf{1}+\mathbf{1'}+\mathbf{2}) \times 100$, exceeding 85%.

To provide more insight on the phenyl migration path and its energetics, ab-initio simulations have been carried out within the density functional theory (DFT) approach. The computational weight has been minimized by reducing the size of the ribbon structure to the minimum relevant representation, which in this case is constituted by a naphthalene unit that accounts for the periphery of the 13 atom wide stripe of Ph-7-13-AGNR, and the phenyl side group (see Fig. S2). The substrate has been represented by a slab containing 4 layers of (4×6)-Au(111) (see Methods for further details).

Figure 3 illustrates the most probable scenario obtained from our comparative analysis of the energetics of different reaction paths (see Figs. S4–S6 for other alternative reaction paths explored, as well as for the energy barrier calculations of representative cases). The phenyl migration reaction mechanism is triggered by a homolytic C-H cleavage at the C_3 site that is promoted by a Au adatom (step **1**). The resulting Au-H bond is then cleaved and the H adatom diffuses away from the interaction region (step **2**). The second internal transformation is the cyclization of the σ radical (step **3**). Both steps, C-H cleavage, and cyclization, are mediated by Au adatoms, as inferred from the significant reduction in the excess energy obtained in the presence of the adatom. For instance, for step **1** we find a reduction from 2.87 eV to 0.77 eV, the latter close to the value obtained for a similar Au adatom-assisted C-H cleavage step[30]. After diffusion of the Au adatom (step **4**), the H on the sp^3 carbon in the intermediate structure **E** can eventually migrate to the C_2 site (step **5**) at very low energy cost, with an energy barrier that is considerably lower than that of the formation of a radialene unit by the migration of the H away from the 4 membered ring (see Fig. S6). This [1,3] sigmatropic H shift triggers the opening of the four-membered ring from the C_2 site, leading to intermediate **G** (step **6**). In a final step, the σ radical of the phenyl that results from the ring opening is passivated by residual H (step **7**), originated either during the phenyl migration reaction, or previously during the cyclodehydrogenation.

All steps with the exception of the last two are endothermic, with the rate limiting one being the cyclization (step **3**) with an excess energy of 1.51 eV. Similar excess energies in the order of 1–2 eV have also been obtained for other on-surface reaction steps that have been experimentally achieved in the temperature range used in our study[24,31,32]. The energy barriers of up to 2.5 eV obtained in these studies are also within the range of those calculated here for steps **1** and **5** (see Figs. S5 and S6), altogether validating our proposed scenario for the thermally induced phenyl migration.

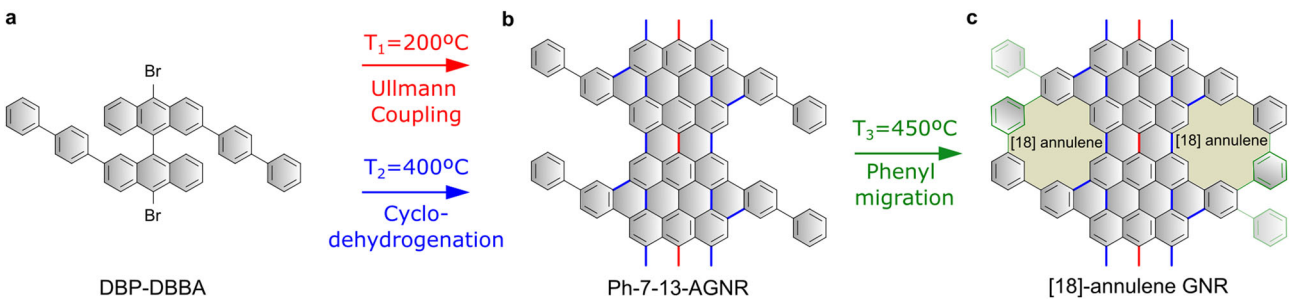

Fig. 1 | Schematic illustration of the synthetic steps for the generation of porous [18]-annulene GNRs. a Molecular structure of the DBP-DBBA precursor. **b** Phenylated nanoribbon Ph-7-13-AGNR obtained after the Ullmann coupling and subsequent cyclodehydrogenation reactions induced at steps T_1 and T_2 respectively. **c** [18]-annulene GNR obtained by the on-surface phenyl migration and dehydrogenative *meta* coupling. The initial position of the migrated phenyl is shown in semitransparent green color.

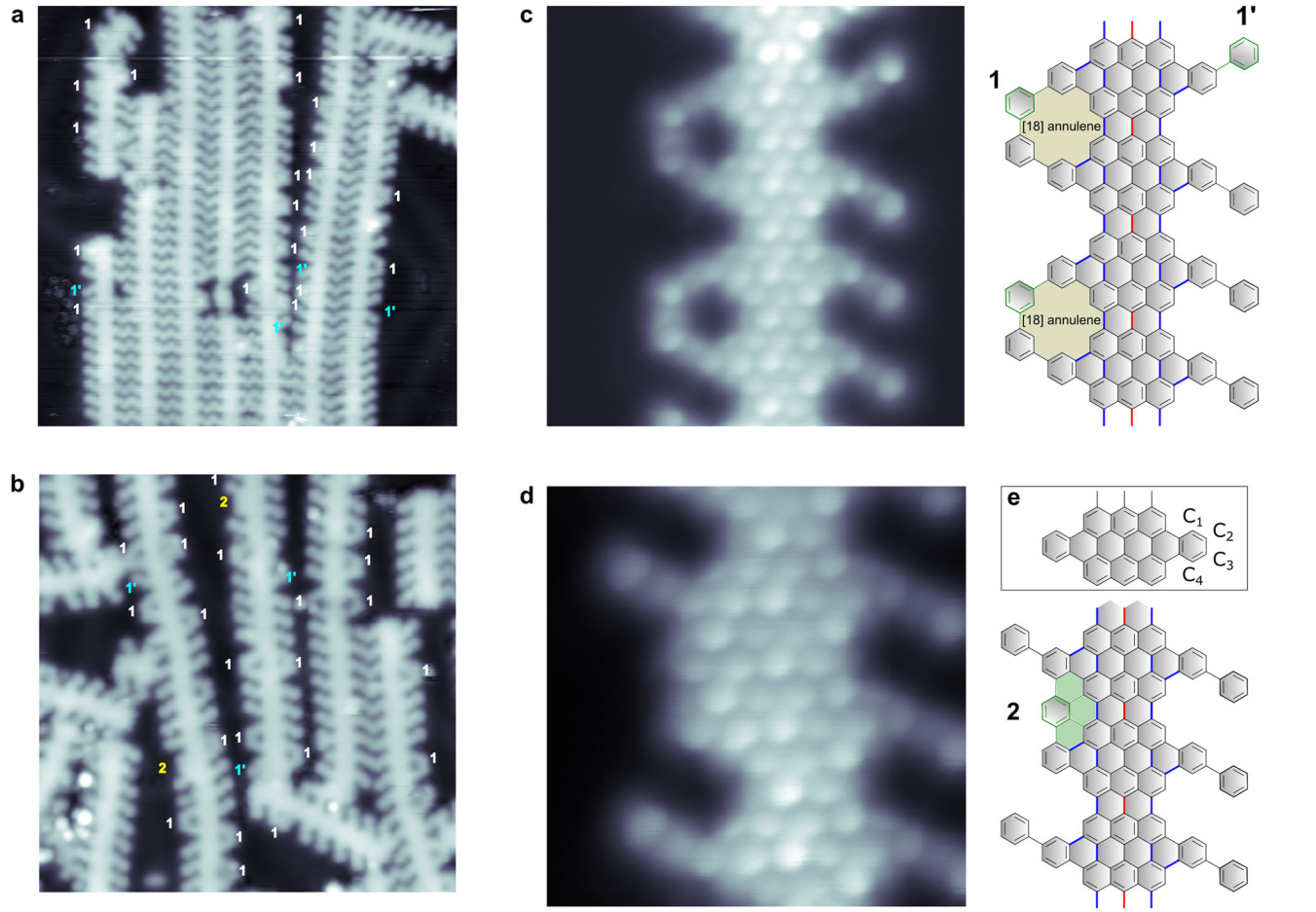

Fig. 2 | Formation of [18]-annulene pores assisted by phenyl migration. STM images of a region of NPG stripes (**a**) and a region of anchored ribbons (**b**) obtained on a flat Au(111) surface after the final annealing step at $T = 450$ °C. The isolated GNRs present different type of phenyl migration assisted edge transformations, labeled as **1**, 1' and **2**. STM image parameters: **a** 40×40 nm^2, $I_t = 0.05$ nA, $V_s = 0.54$ V; **b** 20×20 nm^2, $I_t = 0.1$ nA, $V_s = 0.6$ V. **c** BR-STM image of a GNR section exhibiting the formation of two [18]-annulene pores (**1**), and an unpaired migrated phenyl (**1'**) (4.1×4.1 nm^2, $V_s = 5$ mV). The corresponding atomic structure is sketched at the right. **d** BR-STM image of a GNR section exhibiting the phenyl migration to a C_1 site and its incorporation in the backbone by a triple dehydrogenative coupling (**2**) (2.8×2.8 nm^2, $V_s = 5$ mV). The corresponding atomic structure is sketched at the right. **e** 7-13-AGNR unit indicating the different C sites of the fused benzene ring.

The edge transformation has only subtle effects in the electronic structure of the ribbon, as concluded from our complementary experimental and theoretical analysis. For the former, we combine constant height (CH) spectra to probe frontier bands around the Fermi level, with constant current (CC) spectra to probe the higher energy region where confined states derived from the image potential, also referred as superatom molecular orbitals (SAMO). A comparative analysis of the spectra obtained for sections of pristine phenylated and [18]-annulene edges is summarized in Fig. 4a. The spectra reveal similar values of the valence band maxima (VBM) and conduction band minima (CBM). The gap of ~1.1 eV derived from the spectrum matches that of the non-phenylated 7-13-AGNR[9], meaning that neither the phenyl group nor its specific configuration affect the frontier bands. The only noticeable difference is the additional feature appearing around 0.6 eV at the annulene pore site. This state is more evident in the CC spectra, where the lowest energy features are enhanced by the smaller tunneling gap in this energy region. In this spectrum the coincidence of the CBM and CBM + 1 for both type of edges is confirmed. At higher energy, the prominent peak found at 2.25 eV for Ph-7-13-AGNR coincides in energy with the SAMO found for the non-phenylated counterpart at the bay regions[9]. At the annulene pore, this peak is upshifted by 0.25 eV.

Ab-initio calculations are in line with the main experimental observations (Fig. 4b). The VBM, CBM, and CBM+1 remain unperturbed upon the formation of the annulene pores. The VBM/CBM gap of 0.74 eV obtained for the two cases matches also with that obtained for 7-13-AGNR[9]. The density of states (DOS) of the [18]-annulene-GNR does not show any additional contribution in this energy region, thus the feature found at 0.6 eV in the experimental spectra cannot be assigned to an intrinsic ribbon band. Instead, we attribute the peak to the confinement of the Au(111) surface state, similar to that found at the coves of Chevron type GNRs[33]. With the onset of transversal bands at around 1.5 eV above the Fermi level, the DOS presents many features that undergo some transformation upon the formation of the annulene pores (see Fig. S7 for the full band structure calculations). The STM is, however, most sensitive to the SAMOs that are localized above the ribbon plane. We therefore focus our analysis on these states by identifying them through the projection of the outermost C 3*s* and 3*p* orbitals that are dominant in their eigenstates (shaded areas in Fig. 4b). We locate the onset of the projected states at around 2.92 eV and 3.13 eV for Ph-7-13-AGNR and [18]-annulene-GNR respectively. Despite the higher absolute value as compared to the experimental ones, which is a well-known effect attributed to the surface, the upshift of 0.21 eV is fully consistent with that observed by STM.

The statistical analysis of the products obtained on flat Au(111) surfaces provides direct evidence of the high selectivity in [18]-annulene pore formation. However, the yield is currently limited by the interference of the more favorable lateral inter-ribbon coupling. To enhance this yield effectively, we propose the isolation of GNRs in naturally nanostructured templates, as demonstrated in this study. The periodic array of terraces

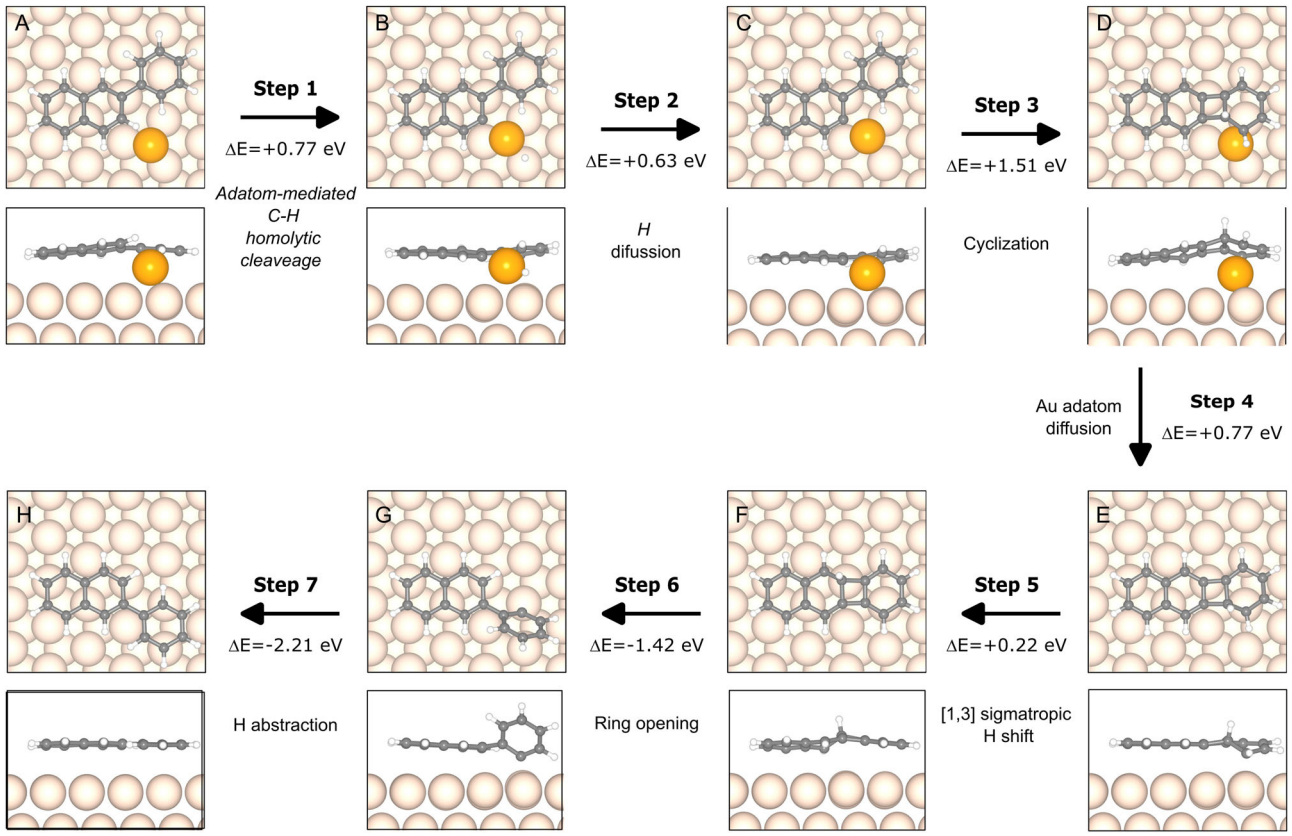

Fig. 3 | Proposed scenario for the phenyl migration pathway based on a DFT energy cost analysis. The GNRs is represented by a naphthalene unit that accounts for the outermost benzene units of the 13 wide stripes of the 7-13-AGNR backbone. The reaction path can be tracked by following the arrows, where the total enthalpy difference between two steps is also indicated. Only two layers of Au are represented in the side views for clarity. C, H and Au atoms are represented by dark gray, blue, and light brown spheres, respectively. Diffused H (from **C** to **H**) and Au (from **E** to **H**) adatoms are out of the region represented in these figures. See Fig. S3 for a representation of the full unit cell.

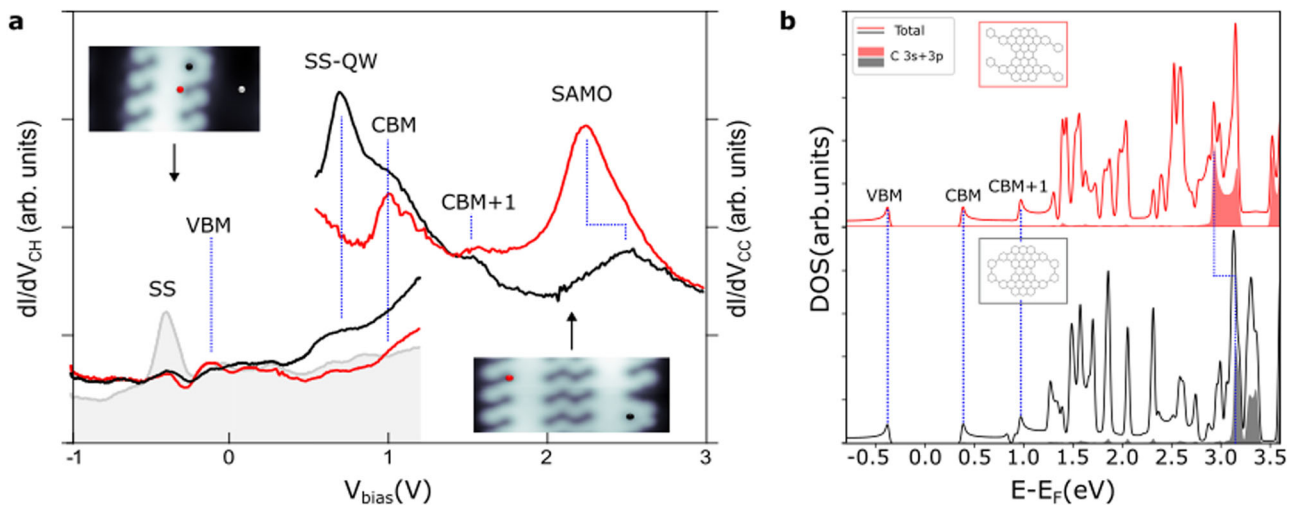

Fig. 4 | Electronic properties of the GNRs before and after the edge transformation. a Constant height (CH, left axis) and constant current (CC, right axis) dI/dV spectra acquired at a phenylated (red) and annulene (black) edge of a ribbon. For the CH series, a reference spectrum acquired on the Au surface is included (shaded gray). The CC spectra has been vertically offset for better visualization. Insets show the corresponding sites where spectra was taken. Parameters: $f = 2.5$ kHz, $V_{mod} = 30$ mV; setpoint for CH spectra: $I_t = 500$ pA, $V_{bias} = -1.0$ V; for CC spectra: $I_t = 11$ pA. **b** Density of states obtained by DFT for a Ph-7-13-AGNR (red) and [18]-annulene-GNR (black). The projection to the outermost C 3s and 3*p* orbitals, representative of the SAMOs, is highlighted in shaded color.

separated by monoatomic steps offered by vicinal surfaces represents an ideal template for that purpose. Vicinal surfaces have already been used for the synthesis of aligned GNRs, enabling the characterization of their anisotropic electronic, optical, and phononic properties through techniques such as ARPES[34,35], photoluminiscence[36], and Raman[37]. Additionally, they have been utilized to optimize the performance of GNR-based field-effect transistors[38]. The well-defined nanometer-scale terraces have also proven valuable in controlling the width of GNRs grown by the lateral fusion of

polyphenylene chains[39]. Leveraging the terrace-confined growth could inhibit the lateral fusion of Ph-7-13-AGNRs, consequently boosting the yield of pore formation on a macroscale.

We have explored this approach by utilizing a curved Au(111) surface for the synthesis of Ph-7-13-AGNRs. The curvature of the surface results in a continuously varying local vicinal angle along the [11$\bar{2}$] direction (steps parallel to [1$\bar{1}$0]). This varying miscut angle facilitates the identification of the optimal terrace size regime for our objectives, specifically the growth of isolated GNRs per terrace at maximum density without compromising the morphology of the GNRs due to limited diffusion along narrow channels. For the 2.5 nm wide Ph-7-13-AGNRs, we determine that the optimum terrace width is around 4–5 nm. Figure 5 summarizes the main observations after the final annealing, increased to $T = 480$ °C in this case to maximize the phenyl migration yield. Above this temperature we begin to observe irreversible damage in the ribbon structure. It is noteworthy that, in addition to the temperature increase, the pore formation yield in the stepped surface may also be affected by the greater availability of Au adatoms on the stepped surface and their role in assisting phenyl migration, as elucidated by our ab initio study. A representative STM image of the surface is presented in Fig. 5a, where GNRs are attached to step edges and consequently aligned by them. The increased pore density is readily apparent. The selective formation of [18]-annulene pores is particularly efficient for the ribbon side that is not interacting with the step edge (outer side). The higher reactivity of the fast diffusing step edge atoms, along with the different local adsorption configuration of the ribbon, seems to result in more irregular pore structures in the ribbon side in contact with the step edge (inner side). We therefore only focus in the well-defined adsorption configuration of the outer side in our statistical analysis, conducted with over 400 phenyls and summarized in Fig. 5b, alongside the values obtained for the flat surface. We find that the selectivity towards the formation of [18]-annulene pores remains above 85%, similar to that found on the flat surface. However, by maximizing the annealing temperature and simultaneously inhibiting the lateral fusion of GNRs through anchoring at step edges, we have achieved the isolation of 100% of the GNRs at densities up to 25×10^4 GNRs/μm, with a yield of [18]-annulene pores exceeding 60% (see Fig. 5b). The absence of unpaired adjacent phenyl rings in the [18]-annulene-GNRs obtained through this procedure suggests that we have reached the stochastic limit in the formation of annulenes.

In summary, in this work we have demonstrated that the phenyl migration can be incorporated into the toolbox of on-surface synthesis reactions in order to trigger internal transformations in graphene nanostructures in a controlled manner. Specifically, we have demonstrated that phenyl migration followed by intraribbon dehydrogenative meta coupling, can selectively induce arrays of [18]-annulene pores at the sides of GNRs. The reaction has been effectively directed towards the pore formation by inhibiting the more favored interribbon coupling through the use of a stepped surface. This strategic approach can be employed to facilitate various other internal reactions that may be hindered by undesirable lateral interribbon interactions, thereby paving the way for extending sequential multistep synthetic schemes to a more complex level.

Methods

Synthesis of the molecular precursors

The solution synthesis of the DBP-DBBA precursor has been reported previously. Full details of the synthesis can be found in ref. 13.

Sample preparation and on-surface synthesis

The Au(111) single crystal was prepared by repeated sputter-anneal cycles using Ar^+ ions at an energy of 1 keV and annealing to 470 °C. Precursors were sublimated from a commercial Dodecon OMBE four-fold Knudsen cell at 355 °C, with the Au(111) sample held at room temperature. The sample temperature was measured by using a thermocouple directly in contact to the sample. The base pressure during evaporation was below 1×10^{-9} mbar. The curved vicinal single crystal obtained from Bihurcrystal S.L. was cleaned by following a similar procedure but using a reduced energy of 0.5 keV for Ar^+ ions.

Experimental details on the imaging method

All STM experiments were carried out using a commercial CreaTec LT-STM held at $T = 5$ K and a base pressure $<5 \times 10^{-10}$ mbar using platinum-iridium tips. Image processing was performed using the WSXM software[40].

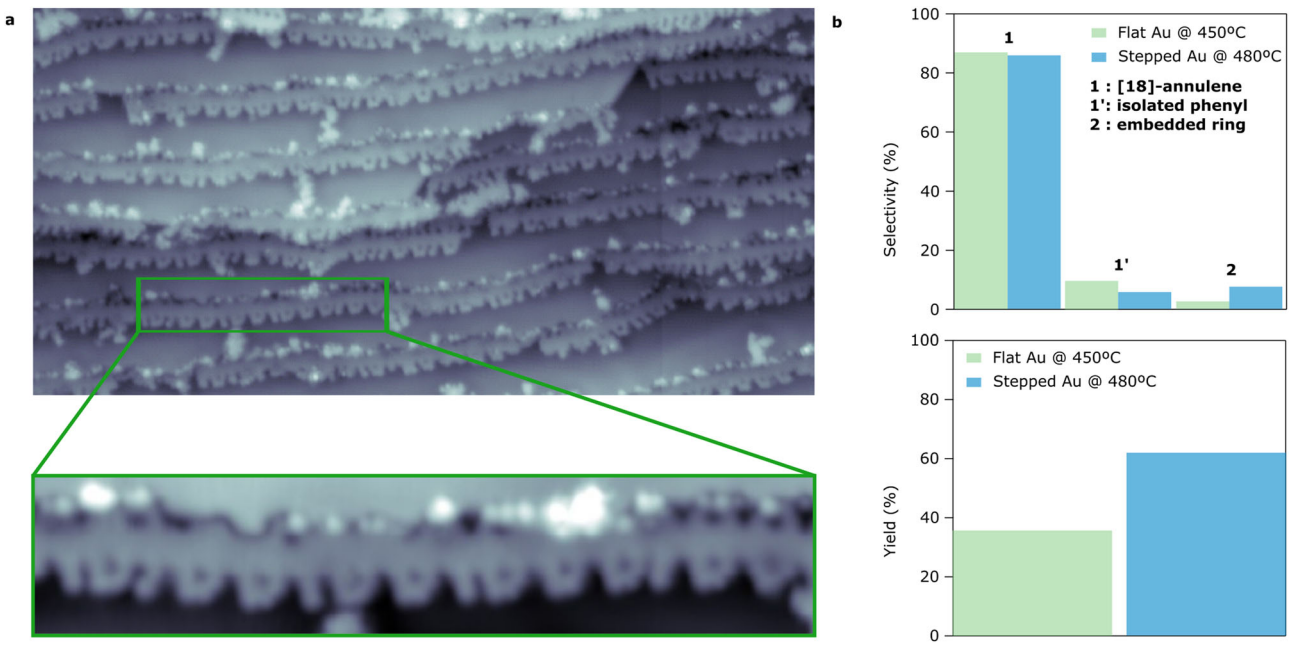

Fig. 5 | Synthesis of [18]-annulene GNRs on a curved Au(111) surface. **a** Representative STM image of the [18]-annulene GNRs obtained after post-annealing at $T = 480$°C (40×80 nm^2, $I_t = 0.06$ nA, $V_s = 8.5$ V). A zoom of a single ribbon where 80% of the phenyls of the outer side are forming [18]-annulene pores (3.7×11.1 nm^2). **b** Statistical analysis of the selectivity (top) and yield (bottom) obtained on the flat Au(111) postannealead at $T = 450$ °C (green), and the curved Au(111) postannealead at $T = 480$ °C (blue). For the analysis of the flat surface we have only considered isolated anchored ribbons found in the disordered region shown in Fig. 2b. Selectivity is measured as $\mathbf{1}/(\mathbf{1}+\mathbf{1}'+\mathbf{2}) \times 100$. The yield accounts for the relative ratio of phenyls forming [18]-annulene pores.

Bond-resolved STM images were acquired by functionalizing the tip with a CO molecule. For that, the molecules were first introduced on the Au surface by dosing the cryostat with CO gas at a pressure of 5×10^{-7} mbar for 30 s with the sample in a temperature range from 5 to 15 K. The CO was then picked up by the tip by applying pulses of 2.5 V at random positions or by gentle tip indentations on the Au surface until the resolution was suddenly improved. Bond-resolved STM experiments were performed in constant-height mode, with the use of a lock-in amplifier, using a modulation voltage of 5 mV at a frequency of 2500 Hz.

Density functional theory calculations

The geometries and energetics were calculated using density functional theory, as implemented in the SIESTA code[41]. With the aim of reducing the computational cost while capturing the relevant chemical-physical interactions, the nanoribbon's structure has been reduced to a minimum model constituted by a naphthalene unit that accounts for the periphery of the 13 atom wide stripe of Ph-7-13-AGNR, and the phenyl side group. We use a supercell description of the system, made up of a slab containing 4 layers of (4×6)-Au(111), with the model molecule on the top Au surface. The bottom Au surface was passivated with hydrogen atoms to quench one of the Au(111)'s Shockley surface states close to the Fermi level[42]. The top Au layer, all the atoms in the phenyl side group and the atoms in the naphthalene that are connected to the phenyl were allowed to relax, while the rest of C and H atoms in the naphthalene were relaxed only in the z (vertical) direction. The system was considered to be relaxed when forces were <0.01 eV/Å, and the dispersion interactions were taken into account by the nonlocal optB88-vdW functional[43]. The basis set consisted of double-ζ plus polarization (DZP) orbitals for C, H, and bulk Au atoms. Au atoms on the topmost layer were treated with a DZP basis set optimized for the description of the (111) surface of Au[44]. We considered a cutoff of 300 Ry for the real-space grid integrations and a Γ point only k-sampling. Reaction pathways were explored with the climbing image nudged elastic band (CI-NEB) method[45–47] by using Vienna ab initio simulation package (VASP)[48]. The projector augmented wave (PAW)[49,50] pseudopotentials and the general gradient approximation[51] in Perdew-Burke-Ernzerholf form (GGA-PBE)[52] and vdW-optB88[53,54] for exchange-correlation energy were employed. A plane-wave cutoff of 400 eV to expand the wave function was considered. We tested the initial and final state geometries for each step, and the ones with lowest energies were selected as the reactants and products in the minimum energy path (MEP). Our NEB calculations were considered converged when all forces were smaller than 0.02 eV/Å. SIESTA and VASP codes used for ground state energy and barrier calculations, respectively, have been compared considering the energy differences obtained in each case for the adatom free C-H cleavage (the adatom-free analog of step **1** of Fig. 3). The two methods lead to similar energy differences (2.87 eV SIESTA versus 2.79 eV VASP), validating our approach.

Data availability

The datasets generated during and/or analyzed during the current study are available from the corresponding author upon reasonable request.

Received: 2 December 2023; Accepted: 28 August 2024;
Published online: 29 September 2024

References

1. Cai, J. et al. Atomically precise bottom-up fabrication of graphene nanoribbons. *Nature* **466**, 470–473 (2010).
2. Clair, S. & de Oteyza, D. G. Controlling a chemical coupling reaction on a surface: Tools and strategies for on-surface synthesis. *Chem. Rev.* **119**, 4717–4776 (2019).
3. Houtsma, R. S. K., de la Rie, J. & Stöhr, M. Atomically precise graphene nanoribbons: interplay of structural and electronic properties. *Chem. Soc. Rev.* **50**, 6541–6568 (2021).
4. Wang, H. et al. Graphene nanoribbons for quantum electronics. *Nat. Rev. Phys.* **3**, 791–802 (2021).
5. Luque-Alled, J. M., Moreno, C. & Gorgojo, P. Two-dimensional materials for gas separation membranes. *Curr. Opin. Chem. Eng.* **39**, 100901 (2023).
6. Cohen-Tanugi, D. & Grossman, J. C. Water desalination across nanoporous graphene. *Nano Lett.* **12**, 3602–3608 (2012).
7. Liu, Y., Dong, X. & Chen, P. Biological and chemical sensors based on graphene materials. *Chem. Soc. Rev.* **41**, 2283–2307 (2012).
8. Danda, G. & Drndić, M. Two-dimensional nanopores and nanoporous membranes for ion and molecule transport. *Curr. Opin. Biotechnol.* **55**, 124–133 (2019).
9. Moreno, C. et al. Bottom-up synthesis of multifunctional nanoporous graphene. *Science* **360**, 199–203 (2018).
10. Jacobse, P. H. et al. Bottom-up assembly of nanoporous graphene with emergent electronic states. *J. Am. Chem. Soc.* **142**, 13507–13514 (2020).
11. Shekhirev, M., Zahl, P. & Sinitskii, A. Phenyl functionalization of atomically precise graphene nanoribbons for engineering inter-ribbon interactions and graphene nanopores. *ACS Nano* **12**, 8662–86699 (2018).
12. Tenorio, M. et al. Atomically sharp lateral superlattice heterojunctions built-in nitrogen-doped nanoporous graphene. *Adv. Mater.* **34**, 2110099 (2022).
13. Moreno, C. et al. Molecular bridge engineering for tuning quantum electronic transport and anisotropy in nanoporous graphene. *J. Am. Chem. Soc.* **145**, 8988–8995 (2023).
14. Zuzak, R. et al. Synthesis and reactivity of a trigonal porous nanographene on a gold surface. *Chem. Sci.* **10**, 10143–10148 (2019).
15. Hieulle, J. et al. On-surface route for producing planar nanographenes with azulene moieties. *Nano Lett.* **18**, 418–423 (2018).
16. Xu, K. et al. On-surface synthesis of a nonplanar porous nanographene. *J. Am. Chem. Soc.* **141**, 7726–7730 (2019).
17. Fan, Q. et al. On-surface synthesis and characterization of a cycloarene: C108 graphene ring. *J. Am. Chem. Soc.* **142**, 894–899 (2020).
18. Su, J. et al. On-surface synthesis and characterization of [7] triangulene quantum ring. *Nano Lett.* **21**, 861–867 (2021).
19. Zhu, X. et al. On-surface synthesis of c144 hexagonal coronoid with zigzag edges. *ACS Nano* **16**, 10600–10607 (2022).
20. Sun, K. et al. On-surface synthesis of nitrogen-doped nanographene with an [18]annulene pore on Ag(111). *Commun. Chem.* **6**, 1–7 (2023).
21. Ammon, M., Sander, T. & Maier, S. On-surface synthesis of porous carbon nanoribbons from polymer chains. *J. Am. Chem. Soc.* **139**, 12976–12984 (2017).
22. Pawlak, R. et al. Bottom-up synthesis of nitrogen-doped porous graphene nanoribbons. *J. Am. Chem. Soc.* **142**, 12568–12573 (2020).
23. Cheng, S. et al. Stepwise on-surface synthesis of porous carbon nanoribbons with notched zigzag edges. *J. Phys. Chem. C* **124**, 756–763 (2020).
24. Yin, R. et al. Step-assisted on-surface synthesis of graphene nanoribbons embedded with periodic divacancies. *J. Am. Chem. Soc.* **144**, 14798–14808 (2022).
25. Qin, T. et al. Synthesis of a porous [14]annulene graphene nanoribbon and a porous [30]annulene graphene nanosheet on metal surfaces. *Angew. Chem. Int. Ed.* **62**, e202306368 (2023).
26. Ajayakumar, M. R. et al. On-surface synthesis of porous graphene nanoribbons containing nonplanar [14]annulene pores. *J. Polym. Sci.* **60**, 1912–1917 (2022).
27. de Oteyza, D. G. et al. Noncovalent dimerization after enediyne cyclization on Au(111). *J. Am. Chem. Soc.* **138**, 10963–10967 (2016).
28. Ruan, Z. et al. Real-space imaging of a phenyl group migration reaction on metal surfaces. *Nat. Commun.* **14**, 970 (2023).
29. Moreno, C. et al. Critical role of phenyl substitution and catalytic substrate in the surface-assisted polymerization of dibromobianthracene derivatives. *Chem. Mater.* **31**, 331–341 (2018).
30. Björk, J. et al. The role of metal adatoms in a surface-assisted cyclodehydrogenation reaction on a gold surface. *Angew. Chem.* **134**, e202212354 (2022).

31. Blankenburg, S. et al. Intraribbon heterojunction formation in ultranarrow graphene nanoribbons. *ACS Nano* **6**, 2020–2025 (2012).
32. Wang, Z. et al. Self-limited embedding alternating 585-ringed divacancies and metal atoms into graphene nanoribbons. *J. Am. Chem. Soc.* **145**, 8445–8454 (2023).
33. Deniz, O. et al. Electronic characterization of silicon intercalated chevron graphene nanoribbons on Au(111). *Chem. Commun.* **54**, 1619–1622 (2018).
34. Linden, S. et al. Electronic structure of spatially aligned graphene nanoribbons on au(788). *Phys. Rev. Lett.* **108**, 216801 (2012).
35. Piquero-Zulaica, I. et al. Electronic structure tunability by periodic meta-ligand spacing in one-dimensional organic semiconductors. *ACS Nano* **12**, 10537–10544 (2018).
36. Senkovskiy, B. V. et al. Making graphene nanoribbons photoluminescent. *Nano Lett.* **17**, 4029–4037 (2017).
37. Passi, V. et al. Field-effect transistors based on networks of highly aligned, chemically synthesized n = 7 armchair graphene nanoribbons. *ACS Appl. Mater. Interfaces* **10**, 9900–9903 (2018).
38. Borin Barin, G. et al. Growth optimization and device integration of narrow-bandgap graphene nanoribbons. *Small* **18**, 2202301 (2022).
39. Merino-Díez, N. et al. Switching from reactant to substrate engineering in the selective synthesis of graphene nanoribbons. *J. Phys. Chem. Lett.* **9**, 2510–2517 (2018).
40. Horcas, I. et al. WSXM: A software for scanning probe microscopy and a tool for nanotechnology. *Rev. Sci. Instrum.* **78**, 013705 (2007).
41. Soler, J. M. et al. The SIESTA method for ab initio order-N materials simulation. *J. Phys. Condens. Matter* **14**, 2745 (2002).
42. Gonzalez-Lakunza, N. et al. Formation of dispersive hybrid bands at an organic-metal interface. *Phys. Rev. Lett.* **100**, 156805 (2008).
43. Klimeš, J., Bowler, D. R. & Michaelides, A. Chemical accuracy for the van der Waals density functional. *J. Phys. Condens. Matter* **22**, 022201 (2009).
44. García-Gil, S., García, A., Lorente, N. & Ordejón, P. Optimal strictly localized basis sets for noble metal surfaces. *Phys. Rev. B* **79**, 075441 (2009).
45. Mills, G., Jónsson, H. & Schenter, G. K. Reversible work transition state theory: application to dissociative adsorption of hydrogen. *Surf. Sci.* **324**, 305 (1995).
46. Henkelman, G. & Jónsson, H. Improved tangent estimate in the nudged elastic band method for finding minimum energy paths and saddle points. *J. Chem. Phys.* **113**, 9978 (2000).
47. Henkelman, G., Uberuaga, B. P. & Jónsson, H. A climbing image nudged elastic band method for finding saddle points and minimum energy paths. *J. Chem. Phys.* **113**, 9901 (2000).
48. Kresse, G. & Hafner, J. Ab initio molecular dynamics for liquid metals. *Phys. Rev. B* **47**, 558 (1993).
49. Vanderbilt, D. & Soft, Phys self-consistent pseudopotentials in a generalized eigenvalue formalism. *Rev. B* **41**, 7892 (1990).
50. Blöchl, P. E. Projector augmented-wave method. *Phys. Rev. B* **50**, 17953 (1994).
51. Wang, Y. & Perdew, J. P. Correlation hole of the spin-polarized electron gas, with exact small-wave-vector and high-density scaling. *Phys. Rev. B* **44**, 13298 (1991).
52. Perdew, J. P., Burke, K. & Ernzerhof, M. Generalized Gradient Approximation Made Simple. *Phys. Rev. Lett.* **77**, 3865 (1996).
53. Klimeš, J., Bowler, D. R. & Michaelides, A. Chemical accuracy for the van der Waals density functional. *J. Phys.: Condens. Matter* **22**, 022201 (2010).
54. Klimeš, J., Bowler, D. R. & Michaelides, A. Van der Waals density functionals applied to solids. *Phys. Rev. B.* **83**, 195131 (2011).

Acknowledgements

This research was funded by the CERCA Programme/Generalitat de Catalunya and supported by the Spanish Ministry of Economy and Competitiveness, MINECO under Contract No. SEV-2017-0706), Grant Nos. CEX2021-001214-S, PID2022-140845OB-C62, PID2022-140845OB-C63, PID2022-140845OB-C66, PGC2018-096955-B-C43, TED2021-132388B-C41 and TED2021-132388B-C42 funded by MCIN/AEI /10.13039/501100011033, PID2022-140827OB-I00 funded by MICIU/AEI/10.13039/501100011033 and by FEDER, the European Union (EU) H2020 program through the FET Open project SPRING (Grant Agreement No. 863098), the FLAG-ERA grant LEGOCHIP (AEI/10.13039/501100011033 Grants No. PCI2019-111890-2 and PCI-111933-2), and Xunta de Galicia (Centro de Investigación de Galicia accreditation 2019-2022, ED431G 2019/03). This study was supported by MCIN with funding from European Union Next-GenerationEU (PRTR-C17.I1) and Generalitat de Catalunya. X.D.d.C., F.G., A.S., and A.G.-L. acknowledge the financial support received from the IKUR Strategy under the collaboration agreement between Ikerbasque Foundation and DIPC on behalf of the Department of Education of the Basque Government. C.M. was supported by Grant RYC2019- 028110-I funded by MICIN/AEI/ 10.13039/501100011033 and by "ESF Investing in your future". M.T. has been supported by Spanish State Research Agency/FSE (ref. BES-2017-08078, project ref. SEV-2013-0295-17-2).

Author contributions

D.P. and M.V.-V. synthesized the monomer precursor. X.D.d.C., F.G., A.S and A.G.-L. performed the ab initio calculations. C.M. and M.T. performed the STM measurements. C.M. and A.M. analyzed the STM data. All authors discussed the results and contributed to the final version of the manuscript, which was drafted by C.M. and A.M.

Competing interests

The authors declare no competing interests.

Additional information

Supplementary information The online version contains supplementary material available at https://doi.org/10.1038/s42004-024-01284-2.

Correspondence and requests for materials should be addressed to César Moreno, Diego Peña, Aran Garcia-Lekue or Aitor Mugarza.

Peer review information *Communications Chemistry* thanks Jinming Cai and the other, anonymous, reviewer(s) for their contribution to the peer review of this work.